JACS
JOURNAL OF THE AMERICAN CHEMICAL SOCIETY
pubs.acs.org/JACS
Article

Light-Enabled Reversible Hydrogen Storage of Borohydrides Activated by Photogenerated Vacancies

Xiaoyue Zhang, Chaoqun Li, Jikai Ye, Xuechun Hu, Wei Chen, Fang Fang, Dalin Sun, Yongfeng Liu,* Xuebin Yu,* and Guanglin Xia*

Cite This: J. Am. Chem. Soc. 2025, 147, 2786−2796

ABSTRACT: Borohydrides, known for ultrahigh hydrogen density, are promising hydrogen storage materials but typically require high operating temperatures due to their strong thermodynamic stability. Here we introduce a novel light-induced destabilization mechanism for hydrogen storage reaction of borohydrides under ambient conditions *via* photogenerated vacancies in LiH. These vacancies thermodynamically destabilize B−H bonds through the spontaneous "strong adsorption" of BH_4 groups, which trigger an asymmetric redistribution of electrons, enabling hydrogen release at near room temperature, approximately 300 °C lower than the corresponding thermal process. By utilizing specially designed "nano-photothermal reactors", which optimize thermodynamic destabilization effect with nanoscale dispersed LiH and create space-confined "hotspots" to enhance hydrogen storage kinetics, we achieve an ultrahigh hydrogen storage capacity of 11.02 wt % H_2 in $LiBH_4$ using only light irradiation. This light-induced destabilization mechanism can also be extended to other alkali metal borohydrides, offering insights for developing solid-state hydrogen storage materials under mild conditions.

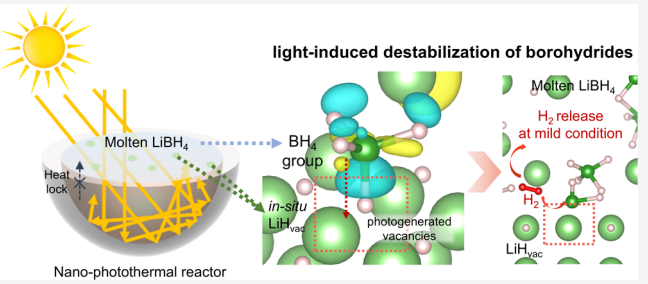

INTRODUCTION

Hydrogen plays a pivotal role in developing a sustainable energy system.[1,2] However, the lack of safe and efficient hydrogen storage substantially impedes the large-scale application of hydrogen energy.[3,4] In this context, lightweight solid-state metal hydrides are considered promising candidates for hydrogen storage owing to their high theoretical hydrogen capacity and safety features.[5−8] Specifically, $LiBH_4$ has theoretical volumetric and gravimetric hydrogen densities of 121 kg H_2 m^{-3} and 18.5 wt % H_2, respectively, making it a highly attractive hydrogen carrier.[9−11] During the dehydrogenation process of $LiBH_4$, it undergoes phase transitions, melting, and decomposition into LiH and B with the release of H_2, as described by the reaction: $LiBH_4 \rightarrow LiH + B + {}^3/_2H_2$. However, in contrast to the exothermic and thermodynamically favorable hydrogenation process, the dehydrogenation of $LiBH_4$ is an endothermic reaction, governed by both high thermodynamic stability and significant kinetic barriers. As a result, harsh reaction conditions are necessitated for reversible hydrogen storage of $LiBH_4$, typically requiring temperatures above 400 °C.[12−14] Although strategies, such as nanostructuring and nanocatalysis, have been developed to reduce its kinetic barriers,[15−18] the operating temperature of $LiBH_4$ remains high, limiting its widespread application until the thermodynamic challenges could be effectively addressed.

Harnessing solar energy, an abundant primary resource, to power chemical reactions is an environmentally friendly solution widely employed in energy harvesting, conversion, and storage.[19−22] Notably, photon-driven chemical processes exhibit unique mechanisms in certain reactions that enable effective modulation of thermodynamics and achieve high catalytic activity and/or selectivity,[23−26] distinguishing them from traditional thermal methods. For example, some organometallic hydrides exhibit photochemical reactivity by breaking metal−hydrogen bonds through charge transfer under illumination.[27] Recently, photocatalytic ammonia formation has been achieved using hydride-mediated photon-generated electrons.[28] Importantly, these light-induced processes enable the reactions to occur under near-ambient conditions, surpassing the thermodynamic constraints of traditional thermal solid−gas and/or solid−liquid reactions. This suggests that light can potentially drive thermodynamically challenging reactions at low cost. However, to the best of our knowledge, there are few reports on effectively breaking thermodynamic and kinetic limitations of the solid-state reactions based on the photon-driven pathway.

Received: November 7, 2024
Revised: January 4, 2025
Accepted: January 6, 2025
Published: January 10, 2025

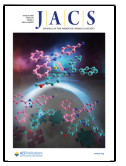

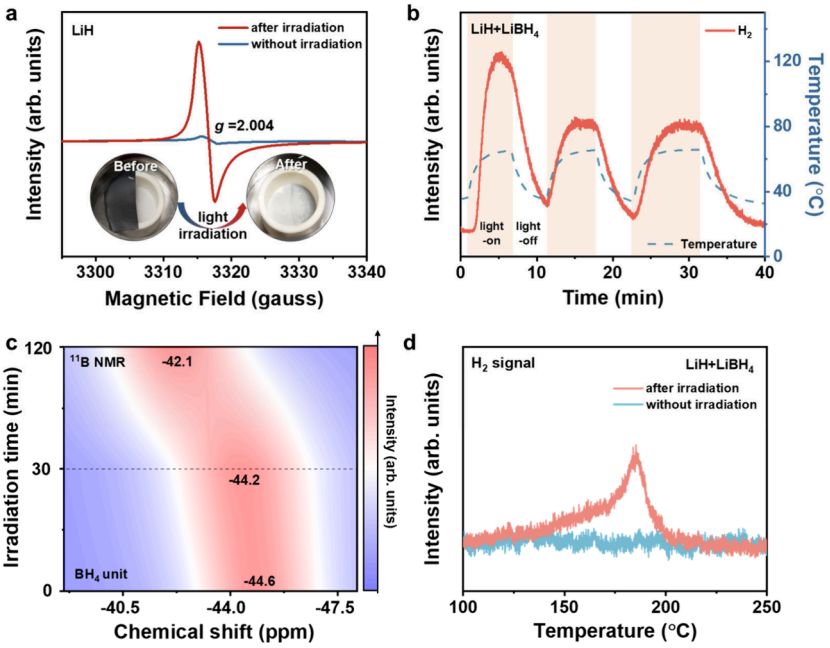

Figure 1. Effects of photogenerated vacancies in LiH on $LiBH_4$. (a) EPR spectra of LiH before and after full-spectrum light irradiation. The insets are the digital photos of pristine LiH (before) and LiH after light irradiation (after). (b) H_2 signal detected by MS from LiH and $LiBH_4$ mixture under light-on and light-off conditions. Sample temperature is continuously monitored in real-time using a contact thermocouple. (c) Solid-state ^{11}B NMR contour plots of BH_4 unit in the LiH and $LiBH_4$ mixture before and after full-spectrum light irradiation at 1 W cm^{-2} over the irradiation period. (d) H_2 signal detected by MS connected with TGA of illuminated LiH and $LiBH_4$ mixture at a heating rate of 5 °C min^{-1}.

Herein, we demonstrate that the thermodynamic and kinetic challenges of hydrogen storage in $LiBH_4$ can be overcome through a novel photon-driven mechanism using LiH. Photogenerated vacancies on LiH create a broader electron localization range, triggering the thermodynamically spontaneous "strong adsorption" of BH_4^- groups and inducing an asymmetric redistribution of electrons that destabilizes the B–H bonds. This process results in a 0.44 eV reduction in enthalpy for thermodynamic destabilization and a 17% decrease in the kinetic barrier compared to traditional thermal catalysis, leading to hydrogen release from solid-state $LiBH_4$ at near room temperature, which is around 300 °C lower than the corresponding thermal process. A mesoporous structured carbon matrix with trace Ni doping, serving as "nano-photothermal reactors" for the loading of $LiBH_4$, is designed to nanoscale-disperse the *in situ* dehydrogenation product LiH, thereby maximizing the thermodynamic destabilization effect. The photothermal effect of ultralow-content Ni-doped structured mesoporous carbon materials (ST-Ni-C) with light scattering property results in the formation of light-permeable molten $LiBH_4$ with low thermal conductivity, and hence the effective creation of localized high-temperature "hotspots" within these "nano-photothermal reactors" for facilitating efficient dehydrogenation of $LiBH_4$. Additionally, the space-confinement effect of structured units prevents phase separation from ST-Ni-C. "Nano-photothermal reactors" represent a pioneering advancement in realizing light-enabled hydrogen storage of borohydrides, enabling $LiBH_4$ to release 11.02 wt % H_2 within just 150 min under light irradiation alone. More importantly, throughout continuous dehydrogenation cycles, the "nano-photothermal reactors" maintain high light absorption and stable nanoconfinement of $LiBH_4$. This preserves the light-induced destabilization effect of vacancies on LiH, resulting in a reversible capacity of 9.40 wt % H_2 for $LiBH_4$ after five cycles. The unique light-induced thermodynamic destabilization effect of photogenerated vacancies on BH_4 groups is universal and can be applied to other alkali metal borohydrides, such as KBH_4 and $NaBH_4$. This work provides a new strategy for developing high-capacity reversible solid-state hydrogen storage materials under mild conditions, contributing to the advancement of a safe and efficient hydrogen economy.

RESULTS AND DISCUSSION

Effects of Light-Induced Vacancies on $LiBH_4$. LiH, as a dehydrogenation product of $LiBH_4$, exhibits a strong absorption peak below 400 nm, indicating its potential for excitation or interaction with ultraviolet (UV) light (Figure S1a). When exposed to full-spectrum light irradiation, the surface of pristine LiH demonstrates a photochromic phenomenon, changing color from white to gray, while unexposed LiH shows no color change (Figure 1a inset). It is confirmed that UV light is responsible for the excitation of LiH, as no color change occurs when LiH is exposed to light filtered for UV wavelengths (Figure S2). This observation aligns with the previous experimental phenomena reported by Chen et al.,[29] where LiH undergoes a minimal photon-driven dehydrogenation reaction under UV irradiation (Figure S1b). Along with the photolysis and trace H_2 release of LiH, hydrogen vacancies are generated as photoexcited electrons are captured at its surface, forming F-centers, which are crystal defects where anion vacancies are occupied by unpaired electrons.[30] As shown in Figure 1a, the irradiated LiH exhibits a sharp and symmetrical signal in the electron paramagnetic resonance (EPR) spectrum with a *g*-factor of 2.004, which indicates paramagnetism due to the unpaired electrons, compared to the nonirradiated LiH, confirming the formation of photogenerated hydrogen vacancies in LiH, referred to as

https://doi.org/10.1021/jacs.4c15744
J. Am. Chem. Soc. 2025, 147, 2786–2796

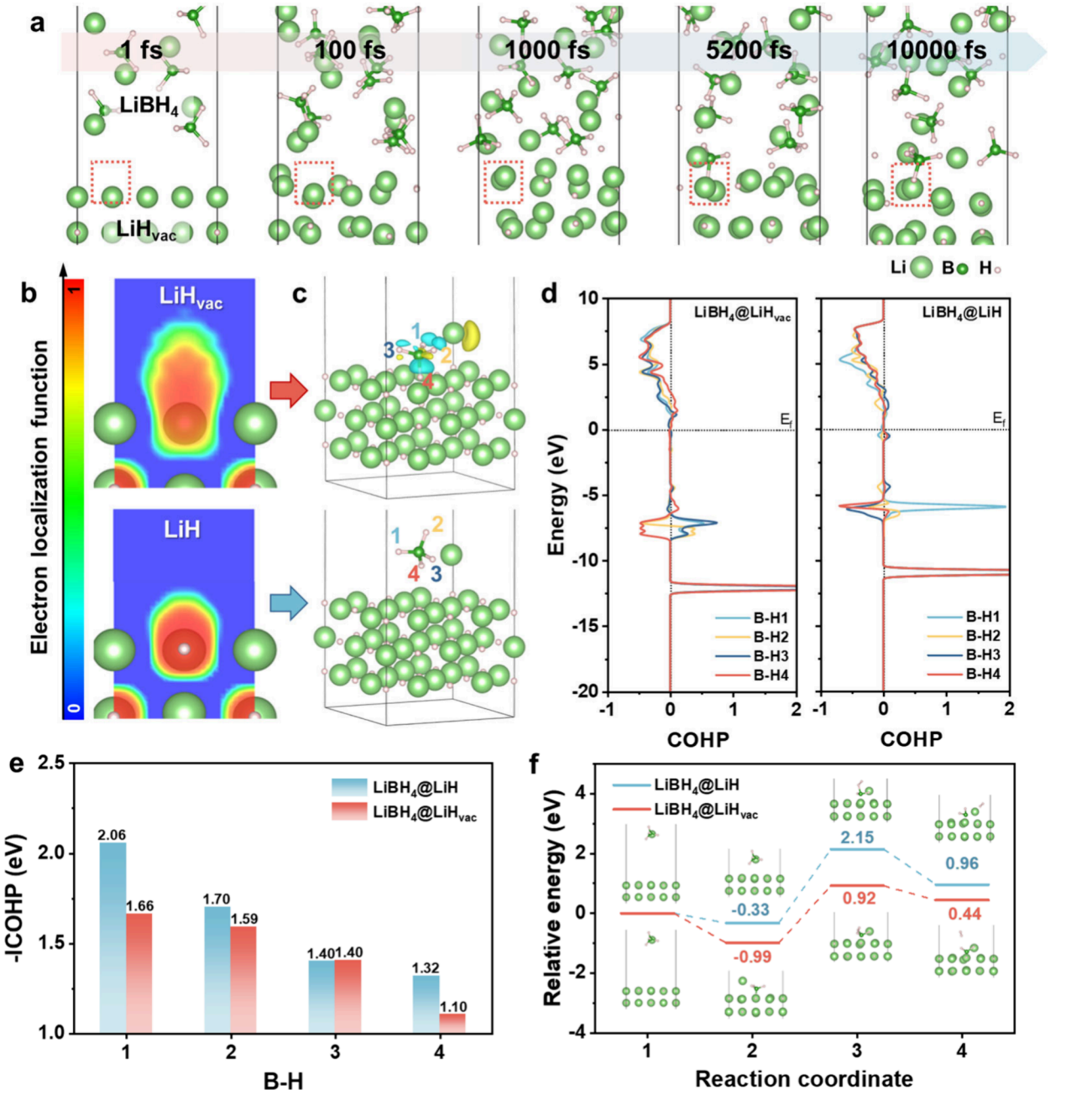

Figure 2. Thermodynamic destabilization and catalytic mechanism of light-induced LiH_{vac} on $LiBH_4$. (a) The *ab initio* molecular dynamics simulation of $LiBH_4$ on LiH_{vac} at 600 K. Lighter green, dark green, and pink spheres represent Li, B, and H, respectively. The dashed red box indicates the position of hydrogen vacancy. (b) The electron localization function of LiH_{vac} and LiH and (c) corresponding migration behavior and charge density difference of the BH_4 group model on them with an isovalue of 0.005 e/Bohr^3. Yellow and blue isosurfaces represent regions of electron accumulation and depletion, respectively. The numbers 1 to 4 represent the four positions of H atoms connected to the B atom. (d) The crystal orbital Hamilton population (COHP) analysis and (e) the value of −ICOHP representing the strengths of the four B−H bonds in $LiBH_4$ on LiH_{vac} (under light irradiation) and LiH (under thermal conditions). (f) Relative energies of $LiBH_4$ on LiH_{vac} and LiH at different reaction states. Reaction coordinate 3 represents the transition state.

light-induced LiH_{vac}. In addition, no significant changes are observed in the XRD patterns before and after irradiation, suggesting that the dehydrogenation reaction, which generates vacancies in LiH, likely occurs primarily on the surface, with an extremely low degree of LiH decomposition (Figure S1c).

To clarify the role of the photogenerated hydrogen vacancies on LiH in promoting the dehydrogenation performance of $LiBH_4$, an equimolar white powder mixture of LiH and $LiBH_4$ is prepared by ball milling for 8 h at the micrometer scale and then exposed to full-spectrum light irradiation. Under a low light intensity of 1 W cm^{-2}, significant H_2 signals are detected by mass spectrometry (MS) upon light illumination, while the surface temperature of the sample is measured at just 66 °C (Figure 1b, Figure S3 and Figure S30). When the sample is heated to 100 °C for 30 min using traditional electric heating, no H_2 signal is observed, confirming that the H_2 release from the LiH and $LiBH_4$ mixture under light exposure is attributed to light-driven decomposition, rather than a thermal effect

https://doi.org/10.1021/jacs.4c15744
J. Am. Chem. Soc. 2025, 147, 2786−2796

induced by the light. To determine the source of the H_2 release, ^{11}B solid-state nuclear magnetic resonance (SSNMR) tests are conducted on samples that have been irradiated over the period under dynamic vacuum. It is revealed that after 30 min of irradiation, a slight downfield shift in the characteristic BH_4 unit could be observed, which becomes more pronounced with extended irradiation with a shift of approximately 2.5 ppm from −44.6 to −44.1 ppm after 120 min (Figure 1c and Figure S1d). This suggests a decrease in the electron density around the boron atoms,[31] likely attributed to a minor loss of hydrogen atoms from the BH_4 groups, meaning the destabilization of $LiBH_4$ occurs at near room temperature under light irradiation. Although the near room-temperature dehydrogenation is partial, this temperature is around 300 °C lower than the corresponding thermal process and even unprecedentedly exceeds the theoretical onset temperature for dehydrogenation determined by the thermal equilibrium, where $LiBH_4$ hardly releases H_2 before 200 °C, as evidenced by the correlation between the equilibrium H_2 release pressure and temperature of $LiBH_4$ in the dark[32] (Figure S4). This destabilization triggers H_2 release under mild conditions, overcoming the thermodynamic limitations of chemical equilibrium in the thermal dehydrogenation of $LiBH_4$.

More interestingly, when performing a further heat-driven TPD dehydrogenation test on the illuminated LiH and $LiBH_4$ mixture, an additional H_2 release signal from $LiBH_4$ is detected at temperatures below 200 °C, which is absent in the sample not exposed to light (Figure 1d and Figure S5). This results in the release of 0.7 wt % H_2 at 191.2 °C occurs 200 °C earlier than the temperature required for the same amount of H_2 release in the sample not exposed to light. A comparison of the heat-driven TPD dehydrogenation results of LiH, with and without light exposure, confirms that over 70% of the H_2 released from the LiH and $LiBH_4$ mixture due to light-induced destabilization below 200 °C is attributed to the dehydrogenation of $LiBH_4$ caused by photogenerated vacancies in LiH, while only approximately 30% comes from the decomposition of LiH. The dehydrogenation behavior of LiH after light exposure in the subsequent heat-driven processes further confirms that light-induced vacancies that are formed upon light irradiation and long-lived even after returning to darkness could thermodynamically destabilize the dehydrogenation of $LiBH_4$ under both illuminated and nonilluminated conditions. It is worth noting that as the relative content of LiH increases, resulting in a higher concentration of photogenerated vacancies in the LiH-$LiBH_4$ mixture, the extent of light-induced destabilization of $LiBH_4$ intensifies (Figure S6). Similarly, as the particle size of LiH decreases with longer milling times for the equimolar LiH-$LiBH_4$ mixture, its expanded surface area also facilitates the formation of more photogenerated vacancies, further leading to enhanced H_2 release through light-induced destabilization under light irradiation (Figure S7). Specifically, the ratio of dehydrogenation amounts from light-induced destabilization below 200 °C to the total H_2 release capacity up to 500 °C increases from 11.97% to 14.40% with the doubling of ball-milling duration, further confirming the role of photogenerated vacancies in LiH in the thermodynamic destabilization of $LiBH_4$. More importantly, similar phenomenon could be observed for the mixed composites of LiH with KBH_4 and $NaBH_4$ (Figure S8). After exposure to light irradiation, these mixtures consistently exhibit dehydrogenation at much lower temperatures, in contrast to the nonirradiated samples. This highlights the universal thermodynamic destabilization effect of photogenerated vacancies on destabilizing BH_4 groups.

To delve deeper into understanding how photogenerated vacancies in LiH affect the dehydrogenation of $LiBH_4$, theoretical calculations are conducted. Initially, *ab initio* molecular dynamics simulations (AIMD) reveal that the BH_4 groups in molten $LiBH_4$ tend to migrate toward hydrogen vacancy sites on the LiH surface after 5200 fs. This process leads to the formation of H_2 from the combination of hydrogen atoms in a single BH_4 group trapped in hydrogen vacancies under sufficient thermodynamic conditions (Figure 2a and Figure S9). Under illumination, hydrogen vacancies that formed on LiH_{vac} capture free electrons (Figure S10), exhibiting an expanded delocalized distribution, as illustrated by the electron localization function (ELF) results (Figure 2b). This generates a strong local electric field at the vacancy site, prompting the "strong adsorption" of BH_4 groups, a thermodynamically spontaneous behavior that reduces the overall energy of the system, clarifying the molecular dynamics migration of BH_4 groups on LiH_{vac} (Figure 2c and f). The charge density difference of trapped BH_4 group in the vacancy site demonstrates significant electron redistribution, while almost no electron transfer is observed in the BH_4 group on LiH without vacancies. In the presence of Li^+ ions in LiH_{vac}, some free electrons interact with H4 trapped in the vacancies, congregating around H4 to enhance its ionic character. This interaction prompts a transfer of the electron cloud from the B−H4 bonds to the vicinity of H4, thereby creating electron depletion zones between the B−H4 bonds. As a result, the B−H4 bonds are destabilized, shifting from covalent to a more ionic character. As electrons decrease in the B−H4 bonds, the σ-bond electrons in the sp^3 hybrid orbitals are depleted, further leading to weakened σ-bond strength and a potential partial shift toward sp^2 or sp hybridization. This alteration further reduces the strength of the B−H1 and B−H2 bonds. Additionally, the remaining free electrons eventually accumulate near the less electronegative Li^+ during the electron redistribution within $LiBH_4$. The crystal orbital Hamilton population (COHP) analysis, aligning closely with the charge density difference results, offers a detailed quantitative depiction of electronic orbital occupancy and bond strengths (Figure 2d). The B−H4 bond shows electron occupancy in lower-energy antibonding orbitals with a widened range of occupancy, leading to a reduction in bond strength from 1.32 to 1.10 eV with a decrease rate of 16.7%. Similar reductions in bond strength for B−H1 and B−H2 are also observed, attributed to increased electron occupancy in lower-energy antibonding orbitals or decreased occupancy in bonding orbitals (Figure 2e).

Furthermore, the relative energies of the dehydrogenation process of $LiBH_4$ on LiH with and without photogenerated vacancies at different reaction states are calculated. With the existence of vacancies in LiH, the enthalpy changes of $LiBH_4$ transitioning from its initial state to BH_2 group upon removal of one H_2 molecule decreases from 0.96 to 0.44 eV, validating that photogenerated vacancies reduce the thermodynamic limits of $LiBH_4$ dehydrogenation. Additionally, the dehydrogenation kinetic barrier of $LiBH_4$ on LiH_{vac} significantly decreases to 1.91 eV, compared to 2.48 eV on LiH. This confirms that photogenerated vacancies in LiH_{vac} also play a catalytic role in promoting $LiBH_4$ dehydrogenation (Figure 2f and Table S1). Theoretical calculations indicate that the photogenerated vacancies on LiH generates electron-rich

https://doi.org/10.1021/jacs.4c15744
J. Am. Chem. Soc. 2025, 147, 2786−2796

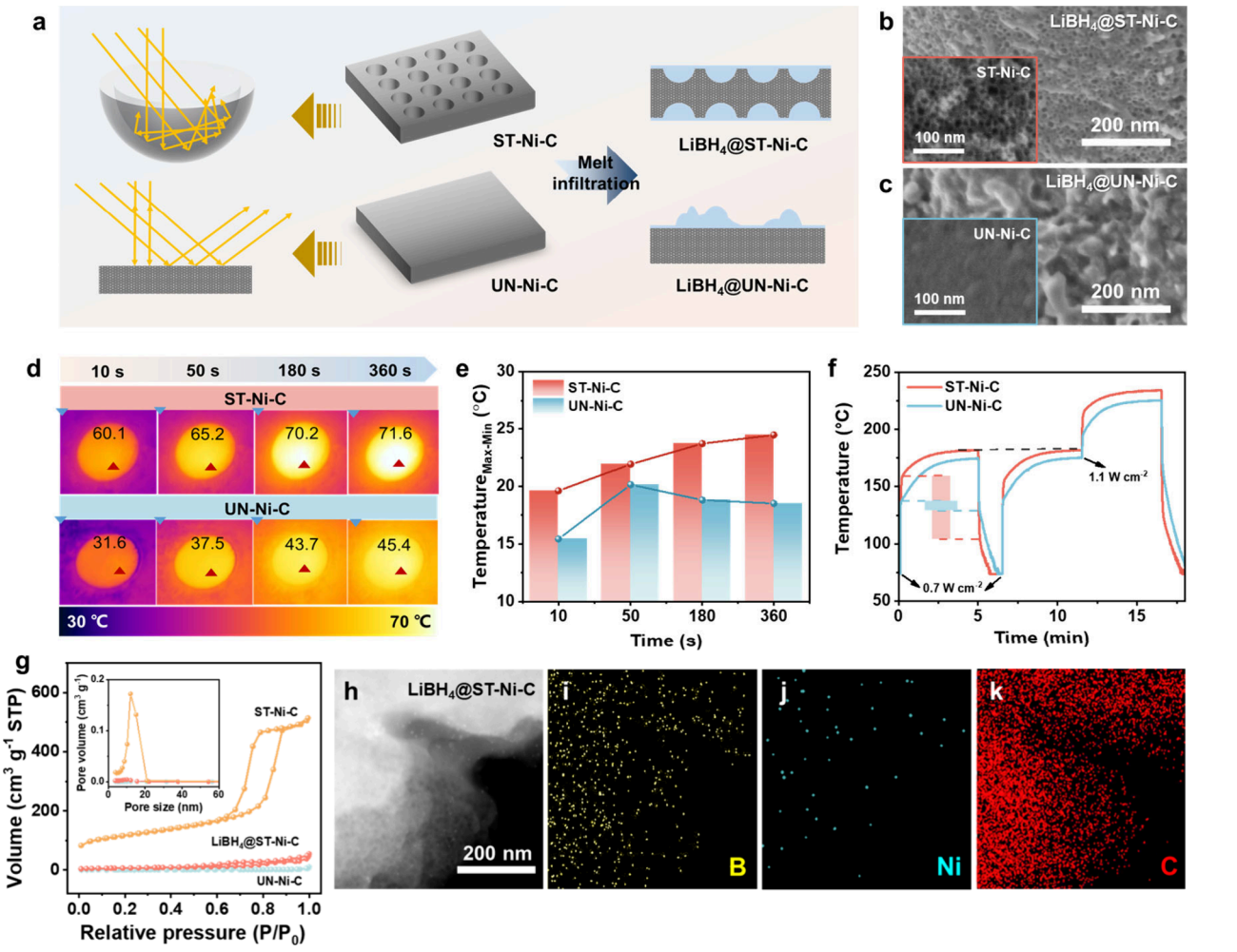

Figure 3. Design and characterization of the "nano-photothermal reactors" for $LiBH_4$. (a) Schematic illustration of the strategic design and fabrication for structured (ST-Ni-C) and unstructured (UN-Ni-C) matrices loaded with $LiBH_4$. SEM images of $LiBH_4$ loaded in (b) ST-Ni-C and (c) UN-Ni-C, with corresponding matrix insets, respectively. (d) *In situ* surface temperatures recorded by an infrared thermal camera under a light intensity of 0.4 W cm^{-2} and (e) corresponding difference between the highest and lowest temperatures within the designated detection area over time for ST-Ni-C and UN-Ni-C. (f) Light response records with surface temperature changes when triggering or removing light irradiation. (g) N_2 isotherm adsorption curves for ST-Ni-C and after loading with $LiBH_4$, and UN-ST-Ni matrix, with corresponding pore size distribution curves inset. (h–k) EDS elemental mapping images of $LiBH_4$ loaded in ST-Ni-C.

regions with expanded electron localization, capturing BH_4 groups and diminishing their structural stability. This interaction destabilizes the B–H bonds and reduces both the thermodynamic and kinetic barriers of the $LiBH_4$ dehydrogenation process. These results suggest the potential of harnessing photogenerated vacancies in LiH, the dehydrogenation product of $LiBH_4$, to enable dehydrogenation of $LiBH_4$ under full-spectrum light irradiation through a unique light-induced mechanism that modifies the reaction's thermodynamics, making it distinct from traditional heat-driven processes.

Design of Nano-Photothermal Reactors for $LiBH_4$. In the previous section, we demonstrated that photogenerated vacancies in LiH could induce the thermodynamic destabilization of $LiBH_4$, and this destabilization increases as the particle size of LiH decreases. However, LiH prepared by ball-milling typically has a particle size on the order of hundreds of nanometers, which limits its effectiveness in destabilizing $LiBH_4$. To further enhance the nanostructuring of LiH and maximize its light-induced destabilization effect on $LiBH_4$, the design of $LiBH_4$-based nanoreactors to obtain nanoscale $LiBH_4$ is proposed. Through this approach, nanoscale LiH could be generated *in situ via* the dehydrogenation reaction ($LiBH_4 \rightarrow LiH + B + {}^3/_2H_2$), thereby maximizing both the light exposure area and the physical contact between light-induced LiH_{vac} and $LiBH_4$. Furthermore, to improve the light-enabled hydrogen storage capacity, it is crucial to fully exploit both the thermal and nonthermal effects of light.[33,34] In addition to the thermodynamic destabilization role of nanosized light-induced LiH_{vac}, these nanoreactors would also enhance light absorption by improving light utilization efficiency, thereby optimizing the conversion of light into thermal energy and further powering the hydrogen storage reaction of $LiBH_4$.

Three-dimensional carbon materials with mesoporous structures, unlike their two-dimensional counterparts that suffer from severe light reflection and rapid heat dissipation, could enhance internal light scattering to promote localized heat concentration within the structures.[35,36] To create a matrix that achieves high temperatures under light irradiation for loading $LiBH_4$, a hard-template method is employed to prepare ultralow-content Ni-doped structured mesoporous carbon materials, designated as ST-Ni-C. As a control, an

https://doi.org/10.1021/jacs.4c15744
J. Am. Chem. Soc. 2025, 147, 2786–2796

unstructured Ni-doped carbon material without a template (UN-ST-C) is synthesized (Figure 3a). Scanning electron microscopy (SEM) images show that ST-Ni-C has tightly packed mesoporous structures (Figure 3b inset), while UN-Ni-C features a flat and smooth surface (Figure 3c inset). High-resolution transmission electron microscopy (HRTEM) images reveal that the pore size of ST-Ni-C is approximately 10 to 20 nm, with no Ni cluster particles formed, as Ni is present in a coordinated form with N and O elements[37] (Figure S11). Energy dispersive X-ray spectroscopy (EDS) elemental mapping indicates a homogeneous distribution of C at 94.4 wt %, along with coordinated elements N, O, and trace amounts of Ni in ST-Ni-C. The mass fraction of Ni, determined to be 0.85 wt % by inductively coupled plasma-optical emission spectroscopy (ICP-OES) analysis (Table S2), confirms that the ST-Ni-C matrix is an ultralow-content Ni-doped mesoporous carbon material.

First, the surface temperatures of ST-Ni-C and UN-Ni-C are monitored over time under full-spectrum light irradiation at 0.4 W cm^{-2} using an infrared camera (Figure 3d). Over a 6-min irradiation period, ST-Ni-C consistently exhibits a higher maximum surface temperature than UN-Ni-C, with a more concentrated distribution of high-temperature zones. Notably, when comparing the temperature differences within the same observation area (Figure 3e), UN-Ni-C initially shows an increase in temperature difference followed by a decline, indicating a slower heating rate and increased heat dissipation during prolonged irradiation. In contrast, the temperature difference of ST-Ni-C continuously increases with irradiation time, suggesting that the heat generated under light irradiation is effectively concentrated within the matrix. These findings demonstrate that ST-Ni-C, with its mesoporous structures, exhibits superior photothermal conversion efficiency, resulting in higher surface temperatures and more pronounced high-temperature zones within the matrix under illumination.

To further assess the impact of mesoporous structures on photothermal performance, the light sensitivity of matrices with and without structured units is evaluated using an infrared thermometer (Figure 3f). Compared to UN-Ni-C, ST-Ni-C reaches a higher temperature more quickly when exposed to light and cools down faster after the light is turned off. This indicates that mesoporous ST-Ni-C responds more rapidly to light due to multiple internal reflections within its structured units, which extend the light path length and enhance the interaction of light with materials,[38,39] highlighting the benefits of intricate internal light scattering. Attributed to the complex light scattering within the structured units, ST-Ni-C exhibits stronger light absorption across the entire spectrum compared to UN-Ni-C, as verified by the ultraviolet−visible-near-infrared (UV-*vis*-NIR) absorption spectra (Figure S12a). Analysis of ST-C without Ni addition confirms that the mesoporous structure is the primary factor enhancing the light absorption capability of ST-Ni-C. Thus, ST-Ni-C maintains a higher surface temperature than UN-Ni-C under the same light intensity, specifically reaching 392 °C under vacuum conditions at 2.8 W cm^{-2} (Figure S12b), which is adequate to drive the dehydrogenation reaction of $LiBH_4$.

$LiBH_4$ is uniformly loaded into ST-Ni-C (or UN-Ni-C) *via* melting infiltration, resulting in $LiBH_4$@ST-Ni-C (or $LiBH_4$@UN-Ni-C). After loading, the porous structural characteristics of ST-Ni-C remain visible, indicating substantial infiltration of $LiBH_4$ into the internal pores (Figure 3b). In contrast, $LiBH_4$@UN-Ni-C exhibits uneven attachment and bulk-like accumulation of $LiBH_4$ on the surface (Figure 3c). Both samples exhibit diffraction peaks corresponding to $LiBH_4$ (PDF#01−076−6069) in X-ray diffraction (XRD) patterns, confirming the successful loading of $LiBH_4$, which is further confirmed by Fourier transform infrared (FTIR) spectroscopy characterization (Figure S13). Benefiting from its porous structures, ST-Ni-C has a significantly higher Brunauer−Emmett−Teller (BET) surface area of 414.4 m^2 g^{-1} compared to UN-ST-C (2.6 m^2 g^{-1}), with all nanosized pores measuring below 20 nm and a total pore volume of 1.58 cm^3 g^{-1}. After loading $LiBH_4$ with a 50% mass fraction, the specific surface area and pore volume of $LiBH_4$@ST-Ni-C decrease to 25.1 m^2 g^{-1} and 0.0084 cm^3 g^{-1}, respectively, reaffirming the effective integration of $LiBH_4$ into the pore structures (Figure 3g and Table S3). In contrast, the small specific surface area of UN-Ni-C leads to a noticeable accumulation of $LiBH_4$ on its surface. Moreover, HRTEM images of $LiBH_4$@ST-Ni-C reveal particles approximately 4.5 nm in diameter, with lattice spacings of 0.196 and 0.210 nm corresponding to the (211) and (002) crystal planes of Ni_2B, respectively, indicating the *in situ* formation of Ni_xB after loading $LiBH_4$ (Figure S14a−c). High-resolution X-ray photoelectron spectroscopy (XPS) spectra provide additional evidence that most of Ni transforms into Ni_xB in $LiBH_4$@ST-Ni-C after loading with $LiBH_4$, as evidenced by the presence of Ni−B bonds in the Ni 2*p* and B 1*s* spectra (Figure S15). There is a uniform distribution of B, Ni, and C, as well as N and O in $LiBH_4$@ST-Ni-C, as indicated by the EDS elemental mapping (Figure 3h-k and Figure S14d-f). These observations prove the successful integration of $LiBH_4$ into the mesoporous carbon ST-Ni-C, along with the *in situ* formation of evenly distributed trace amounts of Ni_xB.

According to differential scanning calorimetry (DSC) curves, pristine $LiBH_4$, initially in the form of a white powder, undergoes a phase change near 110 °C and subsequently melts into a transparent liquid at approximately 290 °C (Figure 4b). Similar phase transitions and melting peaks are observed in $LiBH_4$@ST-Ni-C, with melting occurring before the majority of dehydrogenation. This ensures that incident light penetrates through the molten $LiBH_4$ layer, allowing effective light utilization by the intricately structured matrix during light-enabled dehydrogenation. Notably, after loading with $LiBH_4$, the structured matrix of ST-Ni-C retains its high overall absorbance capability due to the thorough filling of $LiBH_4$ within the pores (Figure S16a). Therefore, $LiBH_4$@ST-Ni-C maintains high light-trapping efficiency and functions as "nano-photothermal reactors" by creating heat "hotspots" within the structured pores.

In addition, pristine $LiBH_4$ exhibits a poor thermal conductivity of 0.764 W m^{-1} K^{-1}, effectively acting as a "thermal insulator" and significantly mitigating heat dissipation caused by thermal conduction (Figure S16b). Although integrating ST-Ni-C into $LiBH_4$ slightly improves the composite's thermal conductivity, potentially aiding heat transfer from the surface downward, the overall thermal conductivity of $LiBH_4$@ST-Ni-C remains relatively low. This implies that the loaded $LiBH_4$ helps to retain the internally generated heat within the structured units. By taking advantage of the light-permeable nature of molten $LiBH_4$ during dehydrogenation and its inherently low thermal conductivity, we successfully developed "nano-photothermal reactors" for $LiBH_4$ that create localized high-temperature "hotspots" under light irradiation, which could promote the thermodynamic

https://doi.org/10.1021/jacs.4c15744
J. Am. Chem. Soc. 2025, 147, 2786−2796

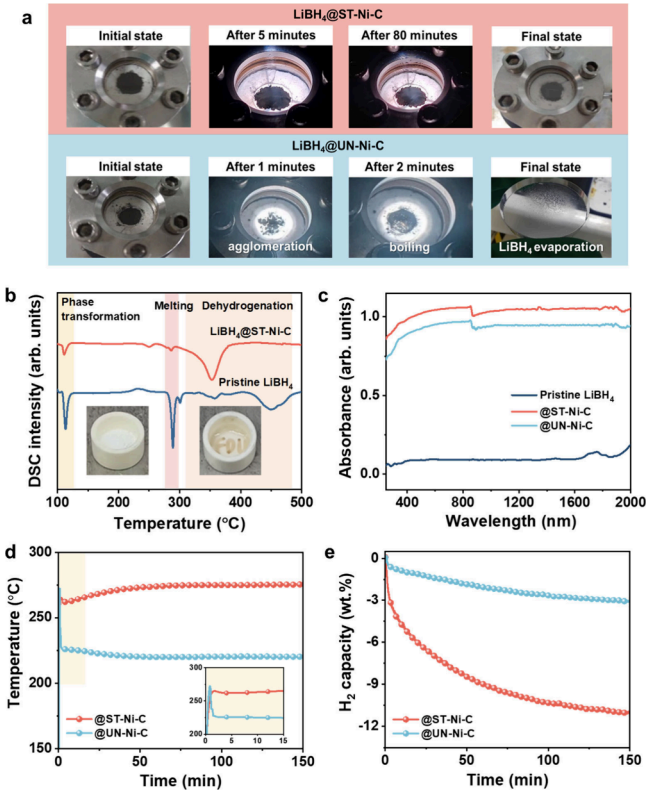

Figure 4. Light-enabled dehydrogenation performance of $LiBH_4$ loaded in ST-Ni-C and UN-Ni-C. (a) Digital photos with an irradiation time of $LiBH_4$ loaded in ST-Ni-C and UN-Ni-C. (b) Programmed-heating DSC curves of $LiBH_4$@ST-Ni-C, including pristine $LiBH_4$ for comparison. The insets are the digital photos of pristine $LiBH_4$ before and after melting. (c) UV−*vis*−NIR absorption spectra and (d) corresponding temperatures of $LiBH_4$ loaded in ST-Ni-C and UN-Ni-C under a light intensity of 3.5 W cm^{-2}. The inset shows an enlarged view of the temperature changes during the first 15 min. (e) Light-enabled H_2 desorption of $LiBH_4$ loaded in ST-Ni-C and UN-Ni-C under a light intensity of 3.5 W cm^{-2}.

destabilization role of light-induced LiH_{vac} for light-enabled $LiBH_4$ dehydrogenation.

Light-Enabled Hydrogen Storage Performance of $LiBH_4$. $LiBH_4$ confined within ST-Ni-C exhibits a significant reduction in dehydrogenation temperature, more than 100 °C lower than that of pristine $LiBH_4$ and $LiBH_4$@UN-Ni-C, along with an accelerated H_2 release rate, as demonstrated by the traditional heat-driven experiments (Figure 4b and Figure S17). Although the presence of trace *in situ* Ni_xB, with a content of 1.95 wt %, contributes to improving the kinetics and reversibility of the $LiBH_4$ hydrogen storage reactions, the improvement is primarily ascribed to the nanoscale space-confinement effect, which enhances the physical contact between $LiBH_4$ and the matrix, effectively suppressing their separation. Therefore, under light irradiation, $LiBH_4$ loaded in structured ST-Ni-C and unstructured UN-Ni-C exhibits markedly different macroscopic behaviors (Figure 4a). In the case of $LiBH_4$@UN-Ni-C, local aggregation begins within the first minute, followed by the rapid formation of bubbles. $LiBH_4$ reaches its boiling point within the next minutes, eventually resulting in a noticeable phase separation from the matrix. This phenomenon corresponds to rapid temperature drops during the initial 2 min, caused by phase separation that exacerbates heat dissipation (Figure S18). In comparison, $LiBH_4$@ST-Ni-C show negligible changes throughout the entire H_2 release process, which indicates that dehydrogenation occurs internally within the structured pores without phase separation. Additionally, coupled with the low thermal conductivity of $LiBH_4$ (Figure S16b), this also helps to maintain localized "hotspots" with high temperatures within the structured pores, thereby promoting more complete dehydrogenation of $LiBH_4$ under light irradiation.

UV-*vis*-NIR absorption spectra indicate that $LiBH_4$@ST-Ni-C maintains higher overall light absorbance compared to $LiBH_4$@UN-Ni-C, meaning the strong light absorption capability of ST-Ni-C is effectively preserved even after with the loading of $LiBH_4$ due to the uniform distribution of $LiBH_4$ within the mesoporous structures (Figure 4c). As the light intensity increases, the surface temperature of $LiBH_4$@ST-Ni-C correspondingly rises, promoting more extensive H_2 release from $LiBH_4$ (Figure S19a−c). When the light intensity is increased to 3.5 W cm^{-2}, the surface temperature of $LiBH_4$@ST-Ni-C reaches 276.2 °C, which is sufficient to drive the dehydrogenation of $LiBH_4$ (Figure 4d). As a result, $LiBH_4$@ST-Ni-C achieves a dehydrogenation capacity of 11.02 wt % H_2 of $LiBH_4$ within 150 min. This is evidenced by the near-complete disappearance of B−H bond peaks in the FTIR spectrum after dehydrogenation, demonstrating almost complete H_2 release from $LiBH_4$ loaded in ST-Ni-C (Figure 4e and Figure S19d). In stark contrast, $LiBH_4$ loaded on UN-Ni-C releases only 3.05 wt % of H_2 with a temperature of only 220.0 °C, highlighting the indispensable role of the "nano-photothermal reactors" in facilitating H_2 desorption from $LiBH_4$ under light irradiation.

To investigate the role of $LiBH_4$ melting in creating "hotspots", a control sample of $NaBH_4$@ST-Ni-C is prepared with the same loading mass as $LiBH_4$@ST-Ni-C *via* the solution impregnation method. In comparison, for $NaBH_4$@ST-Ni-C, even under a higher light intensity of 4.0 W cm^{-2}, the surface temperature only reaches 259.5 °C, which is 16.7 °C lower than that of $LiBH_4$@ST-Ni-C under 3.5 W cm^{-2} (Figure S20). This sample released only 3.78 wt % H_2 after 150 min under 4.0 W cm^{-2}. Given their similar low thermal conductivities,[40] this difference could be attributed to the fact that $NaBH_4$ remains solid during dehydrogenation, filling the pores and preventing light penetration. This highlights the critical role of the light-permeable nature of molten $LiBH_4$ during dehydrogenation for formation of "hotspots" within the "nano-photothermal reactors". While the presence of trace Ni_xB in ST-Ni-C does not contribute to the photothermal effect, it primarily enhances the kinetics of light-enabled $LiBH_4$ dehydrogenation (Figure S21). Additionally, the light-enabled dehydrogenation performance with varying loadings in ST-Ni-C further validates the photothermal and nanoconfinement effects of the "nano-photothermal reactors" (Figure S22).

Subsequently, the mechanisms in thermodynamically and kinetically enhancing the light-enabled dehydrogenation performance of $LiBH_4$@ST-Ni-C driven by photogenerated vacancies in light-induced LiH are investigated. First, to validate the states of hydrogen vacancies, EPR characterization is conducted on the dehydrogenation products of $LiBH_4$@ST-Ni-C, where nanoscale-dispersed LiH is present, after both light-enabled and heat-driven H_2 desorption processes (Figure 5a and Figure S23). A sharp g = 2.004 signal could be found in the light-irradiation sample, which validates the hydrogen vacancies persist even after the light is removed. Although no significant signals are detected in the heat-driven dehydro-

https://doi.org/10.1021/jacs.4c15744
J. Am. Chem. Soc. 2025, 147, 2786−2796

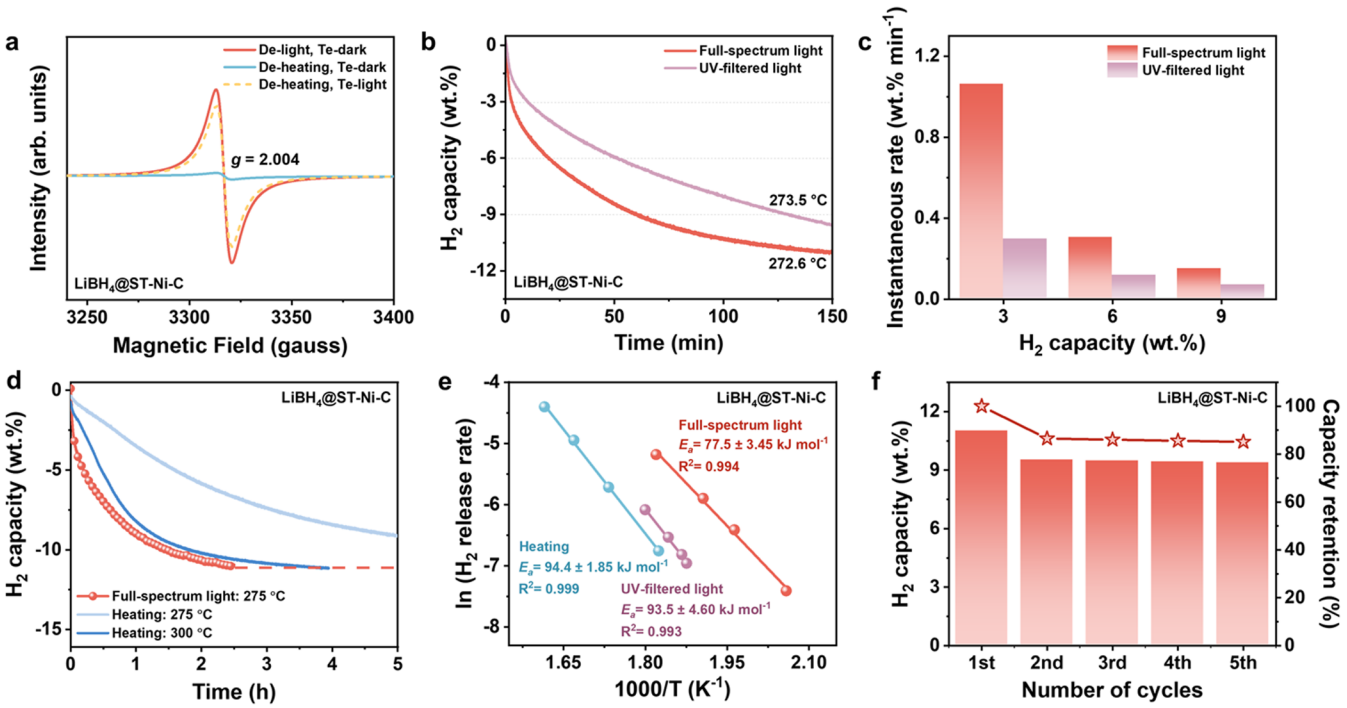

Figure 5. Impact of photogenerated vacancies on light-enabled hydrogen storage performance of $LiBH_4$@ST-Ni-C. (a) EPR spectra of $LiBH_4$@ST-Ni-C after dehydrogenation under various conditions: light irradiation tested in the dark (De-light, Te-dark), thermal conditions tested in the dark condition (De-heating, Te-dark), and thermal conditions tested under light irradiation (De-heating, Te-light). (b) Light-enabled H_2 desorption of $LiBH_4$@ST-Ni-C and (c) corresponding instantaneous rate at different dehydrogenation stages under full-spectrum light (3.5 W cm^{-2}) and UV-filtered light (3.8 W cm^{-2}). (d) H_2 desorption curves of $LiBH_4$ loaded in ST-Ni-C under full-spectrum light (3.5 W cm^{-2}, corresponding to 275 °C) and electrical heating (275 and 300 °C), respectively. (e) Activation energies of $LiBH_4$@ST-Ni-C driven by heating, full-spectrum light, and UV-filtered light. (f) Cycling H_2 desorption capacity with retention of $LiBH_4$@ST-Ni-C after five cycles under 3.5 W cm^{-2} full-spectrum light.

genated product, subsequent *in situ* light irradiation reveals the corresponding signal peak, providing direct evidence to the formation of the hydrogen vacancies induced by full-spectrum light irradiation.

To further verify the impact of light-induced LiH_{vac} on the dehydrogenation performance of the sample, comparative dehydrogenation studies are performed on $LiBH_4$@ST-Ni-C under full-spectrum and UV-filtered light irradiation. At an intensity of 3.5 W cm^{-2} of full-spectrum light irradiation, $LiBH_4$@ST-Ni-C achieves an average temperature of 272.6 °C. Upon increasing the intensity to 3.8 W cm^{-2} after filtering out UV light, a similar temperature of 273.5 °C could be obtained. At identical thermal conditions, the H_2 desorption capacity of $LiBH_4$ loaded in ST-Ni-C under full-spectrum light irradiation consistently outperforms that under UV-excluded light throughout the test period (Figure 5b). Since all the nanosized LiH in $LiBH_4$@ST-Ni-C is *in situ* generated through the dehydrogenation reaction of $LiBH_4$, the instantaneous H_2 desorption rates at different dehydrogenation stages (i.e., 3, 6, and 9 wt %) are compared between the two samples, where LiH content is theoretically equal among them (Figure 5c). It is noted that the dehydrogenation rate of $LiBH_4$ loaded in ST-Ni-C under full-spectrum light irradiation is consistently higher than that under UV-filtered light irradiation, which suggests that the photogenerated vacancies could enhance both the dehydrogenation extent and the rate of light-enabled $LiBH_4$ dehydrogenation.

In addition, comparative desorption profiles of H_2 release from $LiBH_4$@ST-Ni-C are also conducted under both a light intensity of 3.5 W cm^{-2} and corresponding heating conditions to demonstrate the kinetic differences in dehydrogenation under light irradiation and heating conditions (Figure 5d). At this illumination intensity, the temperature of $LiBH_4$ loaded in ST-Ni-C stabilizes at around 275 °C, resulting in a light-enabled H_2 desorption of 11.02 wt % at 150 min. In contrast, the loaded $LiBH_4$ desorbs only 9.10 wt % H_2 under isothermal heating at the same temperature over an extended period of 300 min. Remarkably, the rate of H_2 desorption driven by full-spectrum light is 1.6 times faster than that driven by heating alone at 275 °C, and it is even comparable to the rate at 300 °C, which requires 240 min to reach the same level of H_2 desorption. This observation suggests that, at identical temperatures, $LiBH_4$ demonstrates superior H_2 release performance with accelerated dehydrogenation kinetics under light irradiation compared to thermal activation. More importantly, the light-enabled dehydrogenation of $LiBH_4$ at 275 °C achieves performance comparable to that obtained by heating at 300 °C, suggesting that the photogenerated vacancies play a synergistic role in thermodynamically and kinetically enhancing dehydrogenation performance of $LiBH_4$, distinct from traditional heat-driven processes.

Subsequently, the apparent activation energies for $LiBH_4$@ST-Ni-C under varying light intensities (or temperatures) are determined by fitting the H_2 release curves under both full-spectrum and UV-filtered light irradiation, using the same light-exposure area and mass, and compared with heating results (Figures S17, S19, and S24). The activation energy for dehydrogenation of $LiBH_4$@ST-Ni-C under UV-filtered light is estimated to be 93.5 ± 4.60 kJ mol^{-1}, comparable to that under heating conditions (94.4 ± 1.85 kJ mol^{-1}). Surprisingly, the activation energy decreases to 77.5 ± 3.45 kJ mol^{-1}, a reduction of approximately 17%, under full-spectrum light

https://doi.org/10.1021/jacs.4c15744
J. Am. Chem. Soc. 2025, 147, 2786−2796

irradiation. Although not all LiH in the sample is exposed to light due to the covered bottom part, this reduction indicates that the light-induced LiH_{vac} with abundant photogenerated vacancies could lower the apparent activation energy for $LiBH_4$ dehydrogenation, significantly improving its kinetic performance, which aligns with the catalytic effects predicted by theoretical calculations.

Throughout the cycling process, "nano-photothermal reactors" that load $LiBH_4$ maintain photothermal performance characterized by high light absorption (Figure S25). Concurrently, the nanoconfinement effect and the destabilizing and catalytic role of stably light-induced vacancies in dehydrogenation products LiH are effectively harnessed (Figure S26). Together, these attributes ensure the continuous light-enabled dehydrogenation of $LiBH_4$. Impressively, under a light intensity of 3.5 W cm^{-2} irradiation, the H_2 capacity of $LiBH_4$ loaded in ST-Ni-C remains as high as 9.40 wt %, corresponding to a capacity retention of 85.1% after five cycles (Figure 5f). The decline in capacity could be associated with the minor binding of B with N and C elements and the growth of Ni_xB (Figures S27−S28).

CONCLUSIONS

In summary, we report that photogenerated vacancies on LiH, the *in situ* dehydrogenation product of $LiBH_4$, could trigger the H_2 release of $LiBH_4$ at near room temperature, overcoming the reaction's thermodynamic limits through a unique photon-mediated pathway. Photogenerated vacancies with a strong local electric field induce the thermodynamically spontaneous "strong adsorption" of BH_4 groups, leading to an asymmetric redistribution of electrons ultimately resulting in the thermodynamic destabilization of the BH_4 groups, accompanied by a lower kinetic barrier. Thus, the destabilization and dehydrogenation of $LiBH_4$ occur at approximately 66 °C under only light irradiation. To amplify the light-induced destabilization effect of LiH_{vac} and achieve greater H_2 desorption, the mesoporous structures of the trace Ni-doped carbon material, ST-Ni-C, are specifically designed to support $LiBH_4$, forming "nano-photothermal reactors". These structures create high-temperature "hotspots" due to enhanced light scattering internally through the translucent molten $LiBH_4$, combined with its low thermal conductivity. "Nano-photothermal reactors" also inhibit phase separation of $LiBH_4$ *via* the space-confinement effect. As a result, the light-enabled dehydrogenation of $LiBH_4$ is achieved for the first time, realizing an unprecedented hydrogen release of 11.02 wt % H_2 in just 150 min only under 3.5 W cm^{-2} light irradiation. Additionally, the activation energy for H_2 desorption from $LiBH_4$@ST-Ni-C under full-spectrum light irradiation decreases from 94.4 kJ mol^{-1} (heat-driven) to 77.5 kJ mol^{-1}, significantly improving kinetic performance. The destabilizing and catalytic effects of photogenerated vacancies on light-induced LiH, combined with the "nano-photothermal reactors" that integrate photothermal and nanoconfinement effects, enable continuous light-enabled dehydrogenation of $LiBH_4$, maintaining an H_2 capacity of 9.40 wt % after five cycles.

This work extends light-enabled strategies to borohydrides-based hydrogen storage systems with ultrahigh capacity by innovatively revealing the inherent advantages of molten $LiBH_4$ and its dehydrogenation product LiH, achieving a significant breakthrough in H_2 storage of $LiBH_4$ using only light irradiation. The light-induced thermodynamic destabilization effect on BH_4 groups demonstrated in this work is universal and it could be extended to other alkali metal borohydrides, offering a new strategy for developing high-capacity metal borohydrides under mild conditions and potentially advancing them as safe and efficient hydrogen storage solutions. This study also enriches the functionality and application of photon-assisted alkali metal hydrides and offers new insights for other photochemical reactions.

ASSOCIATED CONTENT

Supporting Information

The Supporting Information is available free of charge at https://pubs.acs.org/doi/10.1021/jacs.4c15744.

Synthesis, characterization, property measurements and theoretical calculations; Figures S1−S30; Tables S1−S3 (PDF)

AUTHOR INFORMATION

Corresponding Authors

Yongfeng Liu − *State Key Laboratory of Silicon Materials and School of Materials Science and Engineering, Zhejiang University, Hangzhou 310027, China;* orcid.org/0000-0002-4002-8265; Email: mselyf@zju.edu.cn

Xuebin Yu − *Department of Materials Science, Fudan University, Shanghai 200433, China;* orcid.org/0000-0002-4035-0991; Email: yuxuebin@fudan.edu.cn

Guanglin Xia − *Department of Materials Science, Fudan University, Shanghai 200433, China;* orcid.org/0000-0002-3493-4309; Email: xiaguanglin@fudan.edu.cn

Authors

Xiaoyue Zhang − *Department of Materials Science, Fudan University, Shanghai 200433, China*

Chaoqun Li − *Department of Materials Science, Fudan University, Shanghai 200433, China*

Jikai Ye − *Department of Materials Science, Fudan University, Shanghai 200433, China*

Xuechun Hu − *Department of Materials Science, Fudan University, Shanghai 200433, China*

Wei Chen − *Department of Materials Science, Fudan University, Shanghai 200433, China*

Fang Fang − *Department of Materials Science, Fudan University, Shanghai 200433, China;* orcid.org/0000-0003-4717-1037

Dalin Sun − *Department of Materials Science, Fudan University, Shanghai 200433, China*

Complete contact information is available at: https://pubs.acs.org/10.1021/jacs.4c15744

Notes

The authors declare no competing financial interest.

ACKNOWLEDGMENTS

This work was financially supported by the National Key R&D Program of China (Grant 2021YFB3802400 to G. Xia), the National Outstanding Youth Foundation of China (Grant 52125104 to Y. Liu), the National Natural Science Foundation of China (Grants U2130208 and 22279020 to G. Xia), and the Science and Technology Commission of Shanghai Municipality (Grant 23ZR1406500 to G. Xia).

REFERENCES

(1) Schlapbach, L.; Züttel, A. Hydrogen-storage materials for mobile applications. *Nature* **2001**, *414* (6861), 353−358.
(2) He, T.; Pachfule, P.; Wu, H.; Xu, Q.; Chen, P. Hydrogen carriers. *Nat. Rev. Mater.* **2016**, *1* (12), 16059.
(3) Yu, X.; Tang, Z.; Sun, D.; Ouyang, L.; Zhu, M. Recent advances and remaining challenges of nanostructured materials for hydrogen storage applications. *Prog. Mater. Sci.* **2017**, *88*, 1−48.
(4) Hassan, I.; Ramadan, H. S.; Saleh, M. A.; Hissel, D. Hydrogen storage technologies for stationary and mobile applications: Review, analysis and perspectives. *Renewable and Sustainable Energy Reviews* **2021**, *149*, 111311.
(5) Orimo, S.-i.; Nakamori, Y.; Eliseo, J. R.; Züttel, A.; Jensen, C. M. Complex hydrides for hydrogen storage. *Chem. Rev.* **2007**, *107* (10), 4111−4132.
(6) Zhang, X.; Sun, Y.; Xia, G.; Yu, X. Light-weight solid-state hydrogen storage materials characterized by neutron scattering. *J. Alloys Compd.* **2022**, *899*, 163254.
(7) He, T.; Cao, H.; Chen, P. Complex hydrides for energy storage, conversion, and utilization. *Adv. Mater.* **2019**, *31* (50), 1902757.
(8) Liu, Y.; Zhang, W.; Zhang, X.; Yang, L.; Huang, Z.; Fang, F.; Sun, W.; Gao, M.; Pan, H. Nanostructured light metal hydride: Fabrication strategies and hydrogen storage performance. *Renewable and Sustainable Energy Reviews* **2023**, *184*, 113560.
(9) Züttel, A.; Wenger, P.; Rentsch, S.; Sudan, P.; Mauron, P.; Emmenegger, C. $LiBH_4$ a new hydrogen storage material. *J. Power Sources* **2003**, *118* (1−2), 1−7.
(10) Zhang, W.; Zhang, X.; Huang, Z.; Li, H.-W.; Gao, M.; Pan, H.; Liu, Y. Recent Development of Lithium Borohydride-Based Materials for Hydrogen Storage. *Adv. Energy Sustainability Res.* **2021**, *2* (10), 2100073.
(11) Kang, J. K.; Kim, S. Y.; Han, Y. S.; Muller, R. P.; Goddard, W. A. A candidate $LiBH_4$ for hydrogen storage: Crystal structures and reaction mechanisms of intermediate phases. *Appl. Phys. Lett.* **2005**, *87* (11), 111904.
(12) Lide, D. R. *CRC Handbook of Chemistry and Physics*; CRC Press, 2004; Vol. 85.
(13) Shao, J.; Xiao, X.; Fan, X.; Zhang, L.; Li, S.; Ge, H.; Wang, Q.; Chen, L. Low-temperature reversible hydrogen storage properties of $LiBH_4$: a synergetic effect of nanoconfinement and nanocatalysis. *J. Phys. Chem. C* **2014**, *118* (21), 11252−11260.
(14) Zhang, X.; Zhang, W.; Zhang, L.; Huang, Z.; Hu, J.; Gao, M.; Pan, H.; Liu, Y. Single-pot solvothermal strategy toward support-free nanostructured $LiBH_4$ featuring 12 wt% reversible hydrogen storage at 400 °C. *Chemical Engineering Journal* **2022**, *428*, 132566.
(15) Ding, Y.; Li, C.; Zhang, X.; Chen, W.; Yu, X.; Xia, G. Spatial Confinement of Lithium Borohydride in Bimetallic CoNi-Doped Hollow Carbon Frameworks for Stable Hydrogen Storage. *ACS Appl. Mater. Interfaces* **2024**, *16* (38), 50717−50725.
(16) Liu, Y.; Chen, W.; Ju, S.; Yu, X.; Xia, G. Stable hydrogen storage of lithium borohydrides via the catalytic effect of Ni_2B induced by thermodynamic destabilization reaction. *Journal of Materials Science & Technology* **2024**, *202*, 192−200.
(17) Zhang, X.; Zhang, L.; Zhang, W.; Ren, Z.; Huang, Z.; Hu, J.; Gao, M.; Pan, H.; Liu, Y. Nano-synergy enables highly reversible storage of 9.2 wt% hydrogen at mild conditions with lithium borohydride. *Nano Energy* **2021**, *83*, 105839.
(18) Zhang, W.; Zhou, L.; Zhang, X.; Zhang, L.; Lou, Z.; Guo, B.; Hong, Z.; Gao, M.; Sun, W.; Liu, Y.; Pan, H. From nanorods to nanoparticles: Morphological engineering enables remarkable hydrogen storage by lithium borohydride. *Nano Energy* **2024**, *130*, 110128.
(19) Zhao, Y.; Gao, W.; Li, S.; Williams, G. R.; Mahadi, A. H.; Ma, D. Solar-versus thermal-driven catalysis for energy conversion. *Joule* **2019**, *3* (4), 920−937.
(20) Gong, E.; Ali, S.; Hiragond, C. B.; Kim, H. S.; Powar, N. S.; Kim, D.; Kim, H.; In, S.-I. Solar fuels: research and development strategies to accelerate photocatalytic CO_2 conversion into hydrocarbon fuels. *Energy Environ. Sci.* **2022**, *15* (3), 880−937.
(21) Gao, C.; Wang, J.; Xu, H.; Xiong, Y. Coordination chemistry in the design of heterogeneous photocatalysts. *Chem. Soc. Rev.* **2017**, *46* (10), 2799−2823.
(22) Hu, X.; Chen, X.; Zhang, X.; Meng, Y.; Xia, G.; Yu, X.; Sun, D.; Fang, F. In Situ Construction of Interface with Photothermal and Mutual Catalytic Effect for Efficient Solar-Driven Reversible Hydrogen Storage of MgH_2. *Adv. Sci.* **2024**, *11*, 2400274.
(23) Li, X.; Wang, C.; Tang, J. Methane transformation by photocatalysis. *Nature Reviews Materials* **2022**, *7* (8), 617−632.
(24) Park, Y.; Kim, S.; Tian, L.; Zhong, H.; Scholes, G. D.; Chirik, P. J. Visible light enables catalytic formation of weak chemical bonds with molecular hydrogen. *Nat. Chem.* **2021**, *13* (10), 969−976.
(25) Constantin, T.; Górski, B.; Tilby, M. J.; Chelli, S.; Juliá, F.; Llaveria, J.; Gillen, K. J.; Zipse, H.; Lakhdar, S.; Leonori, D. Halogen-atom and group transfer reactivity enabled by hydrogen tunneling. *Science* **2022**, *377* (6612), 1323−1328.
(26) Bian, X.; Zhao, Y.; Waterhouse, G. I.; Miao, Y.; Zhou, C.; Wu, L. Z.; Zhang, T. Quantifying the Contribution of Hot Electrons in Photothermal Catalysis: A Case Study of Ammonia Synthesis over Carbon-supported Ru Catalyst. *Angew. Chem.* **2023**, *135* (25), No. e202304452.
(27) Perutz, R. N.; Procacci, B. Photochemistry of transition metal hydrides. *Chem. Rev.* **2016**, *116* (15), 8506−8544.
(28) Guan, Y.; Wen, H.; Cui, K.; Wang, Q.; Gao, W.; Cai, Y.; Cheng, Z.; Pei, Q.; Li, Z.; Cao, H.; et al. Light-driven ammonia synthesis under mild conditions using lithium hydride. *Nat. Chem.* **2024**, *16*, 373−379.
(29) Cheng, Z.; Guan, Y.; Wen, H.; Li, Z.; Cui, K.; Pei, Q.; Wang, S.; Pistidda, C.; Guo, J.; Cao, H.; Chen, P. Light-Driven De/Rehydrogenation of a LiH Surface under Ambient Conditions. *J. Phys. Chem. Lett.* **2024**, *15*, 6662−6667.
(30) Lewis, W. B.; Pretzel, F. Properties of lithium hydride-III. Paramagnetic resonance of color centers. *J. Phys. Chem. Solids* **1961**, *19* (1−2), 139−146.
(31) Łodziana, Z.; Błonski, P.; Yan, Y.; Rentsch, D.; Remhof, A. NMR chemical shifts of ^{11}B in metal borohydrides from first-principle calculations. *J. Phys. Chem. C* **2014**, *118* (13), 6594−6603.
(32) El Kharbachi, A.; Pinatel, E.; Nuta, I.; Baricco, M. A thermodynamic assessment of $LiBH_4$. *Calphad* **2012**, *39*, 80−90.
(33) Zhang, X.; Sun, Y.; Ju, S.; Ye, J.; Hu, X.; Chen, W.; Yao, L.; Xia, G.; Fang, F.; Sun, D.; Yu, X. Solar-Driven Reversible Hydrogen Storage. *Adv. Mater.* **2023**, *35* (2), 2206946.
(34) Zhang, X.; Ju, S.; Li, C.; Hao, J.; Sun, Y.; Hu, X.; Chen, W.; Chen, J.; He, L.; Xia, G.; et al. Atomic reconstruction for realizing stable solar-driven reversible hydrogen storage of magnesium hydride. *Nat. Commun.* **2024**, *15* (1), 2815.
(35) Shi, Y.; Li, R.; Jin, Y.; Zhuo, S.; Shi, L.; Chang, J.; Hong, S.; Ng, K.-C.; Wang, P. A 3D photothermal structure toward improved energy efficiency in solar steam generation. *Joule* **2018**, *2* (6), 1171−1186.
(36) Han, X.; Besteiro, L. V.; Koh, C. S. L.; Lee, H. K.; Phang, I. Y.; Phan-Quang, G. C.; Ng, J. Y.; Sim, H. Y. F.; Lay, C. L.; Govorov, A.; Ling, X. Y. Intensifying heat using MOF-isolated graphene for solar-driven seawater desalination at 98% solar-to-thermal efficiency. *Adv. Funct. Mater.* **2021**, *31* (13), 2008904.
(37) Ju, S.; Ye, J.; Zhang, H.; Wang, W.; Xia, G.; Cui, W.; Yang, Y.; Pan, H.; Yu, X. Recognizing the contrasting role of N, O dual-coordinated single-atom iron catalyst in Li-S and Al-S batteries. *Energy Storage Materials* **2023**, *56*, 1−12.
(38) Li, Y.; Gao, T.; Yang, Z.; Chen, C.; Luo, W.; Song, J.; Hitz, E.; Jia, C.; Zhou, Y.; Liu, B.; et al. 3D-printed, all-in-one evaporator for high-efficiency solar steam generation under 1 sun illumination. *Adv. Mater.* **2017**, *29* (26), 1700981.
(39) Ren, L.; Wang, Y.; Chen, T.; Wang, M.; Xiao, X.; Zhang, Q.; Liu, X.; Xu, W. Scalable and flexible biomass-based porous Juncus effusus fabric for high-efficient solar interfacial evaporation. *Sol. Energy* **2023**, *256*, 191−201.

https://doi.org/10.1021/jacs.4c15744
J. Am. Chem. Soc. 2025, 147, 2786−2796

(40) Sundqvist, B.; Andersson, O. Thermal conductivity and phase diagrams of some potential hydrogen storage materials under pressure. *Int. J. Thermophys.* **2009**, *30*, 1118−1129.

https://doi.org/10.1021/jacs.4c15744
J. Am. Chem. Soc. 2025, 147, 2786−2796